Journal of Materials Chemistry C

PAPER

View Article Online
View Journal | View Issue

Cite this: J. Mater. Chem. C, 2019, 7, 13294

Designing iridate-based superlattice with large magnetoelectric coupling

Tamene R. Dasa,[ab] Lin Hao,[bc] Jian Liu[bc] and Haixuan Xu *[ab]

Received 12th August 2019,
Accepted 4th October 2019

DOI: 10.1039/c9tc04466c

rsc.li/materials-c

The coupling between ferroelectric and magnetic order provides a powerful means to control magnetic properties with electric fields. In this study, we have investigated the magnetoelectric (ME) coupling in iridate-oxide based superlattices employing first-principles density functional theory (DFT) calculations. In particular, we have investigated several oxide superlattices, including $(SrIrO_3)_1$–$(CaTiO_3)_1$ (SIO–CTO) and $(SrIrO_3)_1$–$(BaTiO_3)_1$ (SIO–BTO), with an alternating single layer of SIO and CTO/BTO. We identify a very large ME coupling in SIO–BTO mediated by both lattice and electronic contributions. In comparison, moderate ME coupling constants are found in SIO–CTO. Further electronic and structural analyses reveal that the large ME coupling of SIO–BTO is caused by the large spin–orbit coupling of 5d iridium as well as the significant polarization induced in the SIO–BTO. Interestingly, we find that the ME coupling in SIO–BTO can further be enhanced by modulating epitaxial strain. These results suggest a route to significantly enhance the ME coupling effects, which might be applicable for other materials and practical applications.

I. Introduction

Magnetoelectric (ME) coupling, such as the coupling between ferroelectric and magnetic order in a single device, enables energy-efficient control of magnetic properties with electric fields[1–3] and could prove highly advantageous for many technologically important applications. ME's underlying mechanism comes from the coexistent breaking of spatial inversion and time reversal symmetry, which is quite rare, especially in a single-phase material.[4,5] There have been several studies focusing on introducing ME coupling in complex oxides.[6–9] For example, an external strain was employed to trigger ferroelectric order into a paraelectric antiferromagnet, $CaMnO_3$, giving rise to an interesting ME coupling.[9] In another study, ferroelectric distortions were employed to introduce weak ferromagnetism and polarization to achieve ME coupling.[6,9,10] However, most of the studies have focused on single-phase oxides. In this study, we propose to achieve ME coupling by building artificial crystal structures, *e.g.*, oxide superlattices, which have the potential to create/combine various ferroic orders at the atomic scale.[11,12] Specifically, in these superlattices, one can gain control of structural distortion and/or symmetry breaking *via* interface engineering which can be introduced by manipulating the cation compositions.[11–14]

Due to the delicacy of measuring the full ME coupling tensor experimentally, there have been theoretical efforts to obtain these ME constants. One of the most widely used techniques is the first principles density functional theory (DFT) approach.[15,16] To extract the electronic ME coupling, a method that quantum-mechanically treats external magnetic/electric fields[16] has been developed. A few studies have been carried out to determine the individual electronic and ionic contributions of ME coupling. One example is the unexpected dominant role of the electronic contribution to the ME properties of FeS.[17] In addition, large electronic contribution to ME coupling is found in Cr_2O_3.[15,16] Since ME coupling originates from the interplay of multiple degrees of freedom, such as electron charge, spin, orbital moments, and structural distortions,[15–20] spin–orbit coupling (SOC) may significantly alter the ME coupling.[21,31] While most studies have focused on 3d transition metal compounds, SOC strength is known to scale with the atomic number, leading increasing interests in 5d transition metal oxides.[22–25] A prototypical system is the iridates, where the Ir 5d orbitals in the oxygen octahedra of iridates have a spin–orbit-entangled pseudo-spin state, which is coupled to orbital moments and is expected to be more susceptible to structural changes or other external stimuli.[21]

In this research, we explore and examine the effects of SOC, structural distortions, and cation effects on the ME coupling in several iridate-based superlattices using DFT. First, the fundamental properties including structural, electronic, and magnetic properties of three iridate superlattices, namely $[(SrIrO_3)_1$–$(SrTiO_3)_1]$ (SIO–STO), $[(SrIrO_3)_1$–$(BaTiO_3)_1]$ (SIO–BTO), and $[(SrIrO_3)_1$–$(CaTiO_3)_1]$ (SIO–CTO) are presented. For these oxide superlattices, we calculate the complete ME coupling tensors using first principle techniques. We compare the various ME responses of these superlattices and examine the effects of epitaxial strains on the ME coupling constants

[a] Department of Materials Science and Engineering, The University of Tennessee, Knoxville, USA. E-mail: xhx@utk.edu
[b] Joint Institute of Advanced Materials, The University of Tennessee, Knoxville, USA
[c] Department of Physics and Astronomy, The University of Tennessee, Knoxville, USA

of SIO–BTO. We analyze the effects of the strong SOC and structural distortions in relation to the variations of the ME coupling constants.

II. Methodology and computational details

The DFT calculations are performed using the Vienna *ab initio* Simulations Package (VASP)[25] with the projector-augmented wave (PAW) method.[26] For the exchange–correlation functional, we use the Perdew–Becke–Ernzerhof revised for solids (PBEsol).[27] The cut-off energy is 600 eV based on convergence tests. For a proper description of the electronic correlation effects, we have included Hubbard correction to the 5d and 3d orbitals of Ir and Ti, respectively. The values of U and J for Ir are 2.2 eV and 0.2 eV, respectively. Similarly, the values of U and J for Ti are 6 eV and 0.64 eV.[25,28] Indeed, the values of the Hubbard correction U can be determined by using non-empirical techniques.[29,30] We have employed an in-plane lattice constant of STO (3.94 Å) for the superlattices, assuming the superlattices be supported by a STO substrate.[31–33] The magnetic field is applied self-consistently and the calculations are done in a non-collinear spin arrangement by including SOC.[16] Detailed description of the implementation of the magnetic field within the Kohn–Sham scheme is discussed in ref. 16. The electron polarizations under finite magnetic fields are calculated using the Berry-phase approach[34] with the positions of the ions frozen. Under magnetic fields, the coupling between the lattice and the magnetization *via* SOC changes the polarization of the superlattices. To compute the changes in the ionic polarizations as a result of the magnetic fields, we perform ionic relaxations in the presence of finite magnetic fields. This quite challenging, computationally. Therefore, we multiply the ionic displacements by the Born effective charges[25,34] to get ionic polarizations as well as magnetoelectric coupling constants. The forces induced by the applied magnetic fields on the ions are rather small; rigorous convergence criterion of the ionic forces is needed. In this study, the ionic forces are reduced to ~ 5 μeV Å^{-1}.

III. Results and discussions

III.A Structural, electronic and magnetic properties of iridate based superlattices

The structural stability of all the iridate-based oxide superlattices in this study has been systematically examined. For instance, to determine the most stable structure of SIO–BTO, various initial structures with different oxygen octahedra rotational patterns, *i.e.* rotation angles and tilting angles, are explored and relaxed using DFT. The energetics of the obtained structures are analyzed to find the most stable structure. A thorough structural analysis of the obtained SIO–BTO is then carried out using the SYMMODES tool.[35] Similar processes have also been applied to SIO–CTO and SIO–STO for comparison, and electronic/magnetic properties are determined based on the obtained ground state structures of these superlattices.

SIO–BTO exhibits a *P*4*bm* ground state, which transits from the centrosymmetric structure (*P*4*mm*) by one polar (Γ_1) mode and one rotational (M4) mode of the oxygen octahedra. The ground state structure of SIO–BTO has an $a^\circ b^\circ c^-$ rotational pattern where IrO_6 and TiO_6 rotates out-of-phase around the *z*-axis. A prominent in-plane rotation angle of 11.8° is observed for IrO_6 octahedra, while the rotation angle of TiO_6 octahedra is considerably weaker, $\sim 1.6^\circ$. The magnetic moments of Ir in SIO–BTO are primarily ordered in an antiferromagnetic manner along the *y*-axis, while a spin-canting-induced net magnetic moment along the *x*-axis is also found (Fig. 1c). The projected magnitude of the magnetic moment on the *y*-axis is 0.43 μ_B, and the net in-plane canting moment is 0.1 μ_B (more details in Table 1). Note that the spin-canting-induced net moment in iridates is well known to be a consequence of the Dzyaloshinskii–Moriya interaction[36,37] in the presence of an in-plane rotation of IrO_6 octahedra or tilting angle.[38–41] In this particular superlattice, there is no out-of-plane net moment because octahedral tilting is absent, which agrees with our recent study in ref. 33 and the reports on collinear antiferromagnet, $Sr_3Ir_2O_7$.[42,43] Analyzing the magnetic structure, we found that SIO–BTO has a magnetic point group of $m'm2'$. SIO–BTO has the

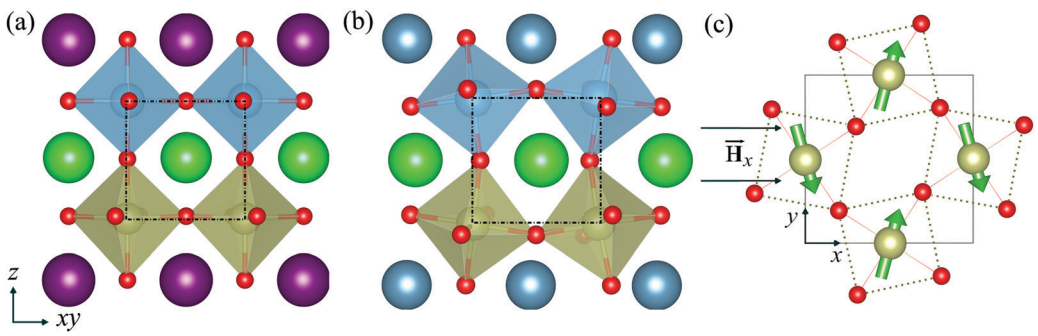

Fig. 1 The structural geometries of (a) SIO–BTO and (b) SIO–CTO. (c) Illustrations of the in-plane magnetic structure of the IrO_2 layer in the SIO–BTO superlattice. The directions of the magnetic moments for two adjacent Ir atoms on the *y*-axis are opposite from each other whereas both Ir magnetic moments are canted towards the *x*-axis. Schematics of a magnetic field applied to compute the magnetoelectric coupling. In these plots, red and gold spheres represent oxygen and Ir atoms, respectively. The A-site cations Sr, Ba, and Ca are represented with green, violet, and blue spheres, respectively.

Table 1 The projected magnitude of Ir total magnetic moments on *x*, *y*, and *z* axes for SIO–BTO and SIO–CTO

		m_x (μ_B)	m_y (μ_B)	m_z (μ_B)
SIO–BTO	Ir_1	0.11	0.43	0.0
	Ir_2	0.11	−0.43	0.0
SIO–CTO	Ir_1	0.08	0.34	−0.1
	Ir_2	0.08	−0.34	−0.1

largest orbital moments among the iridate superlattices in this study.

The ground state structure of SIO–CTO belongs to the *Pc* space group, which has multiple distortion modes from the centrosymmetric structure. Specifically, it undergoes one translational mode (Γ_5), one rotational mode, and a hybrid mode that has both rotational and translational features. An in-phase octahedral rotation between the IrO_6 and TiO_6 octahedra is observed along the *z*-axis. The rotation angle of IrO_6 octahedra in SIO–CTO is $\sim$13.3°. The rotation angle of TiO_6 octahedra is comparatively smaller, about 10.4°. Unlike the SIO–BTO, a strong tilting is observed in SIO–CTO, and the octahedra tilting angle is 15.3°. In accordance with the structural distortion pattern, SIO–CTO has both in-plane and out-of-plane spin canting moments. The net canting moments along the *x*-axis and *z*-axis are 0.08 μ_B and −0.1 μ_B, respectively. These magnetic configurations of SIO–CTO indicate that it has a magnetic point group of m'.

The structure of SIO–STO has the $P2_1/c$ space group, consistent with our recent study in ref. 33, which undergoes three Γ_1 translational modes and one rotational mode from the high-symmetry cubic structure. The optimized structure of SIO–STO has in-plane octahedra rotation where Ir- and Ti-centered oxygen octahedra have opposite angular rotation. The IrO_6 octahedra in SIO–STO has an octahedra rotation of 14.2°, which is larger than the corresponding rotational angle of IrO_6 in SIO–BTO (11.8°). A significant tilting angle also exists in the SIO–STO superlattices, which is much smaller than that of SIO–CTO, implying that the latter superlattice has a dominant out-of-plane canting moment.

We determine the electronic structure of the aforementioned iridate superlattices and analyze the change in the band structures as a result of cation substitution. Both SIO–BTO and SIO–CTO have an intrinsic polarization (ferroelectric order) due to the dissimilar cations in the A-site. In comparison, there is no polarization in the SIO–STO.

The band structures of SIO–STO are plotted in Fig. 2(a). We find the valence bands are dominated primarily by Ir 5d bands, and they are relatively less dispersive as compared with similar bands in SIO–CTO (as shown in Fig. 2(b)). SIO–STO has an indirect band gap of $\sim$0.4 eV, and the valence bands, close to the Fermi energy, are degenerate. We have systematically calculated and analyzed the band structure of cubic, rotated, and tilted SIO–STO, respectively. For instance, the cubic structure without octahedra distortion has a metallic band structure. Octahedra tilting in SIO–STO could create a small band gap. A significant band gap is observed when the IrO_6 octahedra are rotated. Therefore, octahedra rotation is an important structural distortion that can significantly affect the electronic properties and potentially other properties.

The corresponding band structures of SIO–CTO and SIO–BTO are plotted in Fig. 2(b) and (c), respectively. Unlike SIO–STO, the degeneracy in the valence band of SIO–CTO is significantly lifted, especially along *Z*–*Γ*–*U* path of the Brillouin zone. Similarly, the valence bands of SIO–BTO just below the Fermi energy are split at the zone boundary of *Z* and *U*. Since SIO–BTO and SIO–CTO are polarized due to the breaking of inversion symmetry from the different A-site and B-site cations in superlattices, the observed band splitting in both superlattices is related to such polarization. Additionally, the valence band of SIO–BTO is more dispersive than the other two. In other words, electrons in SIO–BTO are less localized than those of SIO–STO and SIO–CTO. Consistently, SIO–BTO has the smallest band gap when compared to SIO–STO and SIO–CTO.

III.B Magnetoelectric coupling in SIO–BTO and SIO–CTO

The origin of the SIO–BTO superlattice's polarization could be related to the ferroelectric order in BTO as well as to the dissimilar cations in the sublattice of SIO and BTO, which lead to structural distortions in the superlattices. The polarization in SIO–BTO, which is directed along the *z*-axis, is obtained from

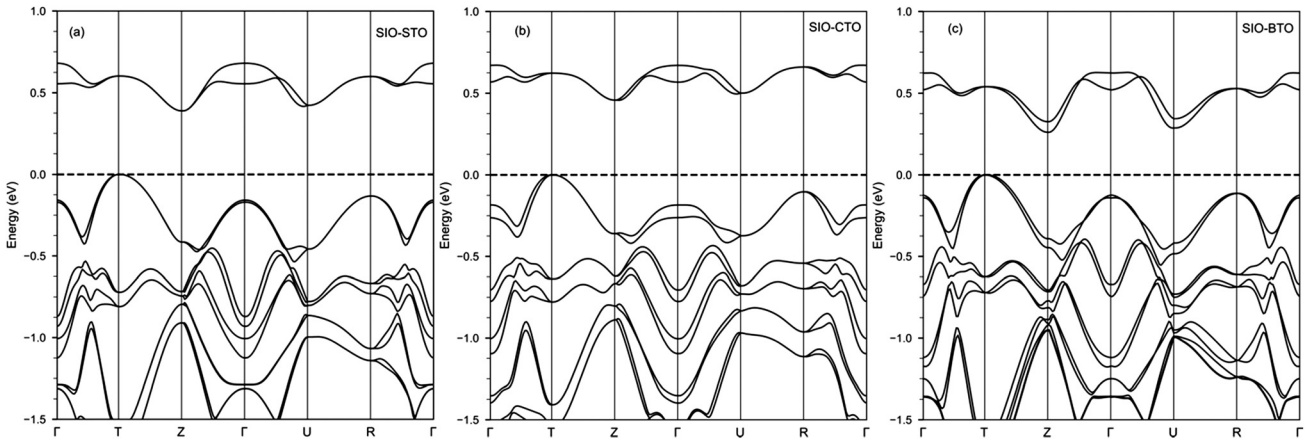

Fig. 2 Band structures of (a) SIO–STO, (b) SIO–CTO, and (c) SIO–BTO obtained from DFT calculations using PBEsol with Hubbard corrections.

Born-effective charge tensor analysis. The value of the polarization is found to be 9.32 μC cm^{-2}. In ferroelectric materials such as those in our study, the magnetic order is commonly considered to be coupled with the ionic polarization,[12] leading to ME coupling. Since the magnetic ordering in SIO–BTO has point group $m'm2'$, there are two possible non-zero matrix elements in the ME coupling tensor, namely β_{zx} and β_{xz} as:

$$\beta = \begin{pmatrix} 0 & 0 & \beta_{zx} \\ 0 & 0 & 0 \\ \beta_{xz} & 0 & 0 \end{pmatrix}$$

The changes in the electronic and ionic polarization induced by the application of a magnetic field along the *x*-axis and *z*-axis are shown in Fig. 3(a) and (b), respectively. Note that the electronic and ionic ME coupling constants were calculated separately. To investigate the electronic contribution of the ME coupling, the ionic positions were fixed and the change of polarization was calculated as a function of the magnetic field. Along this line, magnetic fields were applied along all three directions separately, and the full tensor was then determined by evaluating the corresponding changes in polarization. When a magnetic field is applied along the *y*-axis, neither the electronic or ionic components of the polarization changes, therefore the corresponding ME coupling constants are essentially zero and will not be further discussed.

As shown in Fig. 3(a), the change in the electronic polarization of SIO–BTO has a linear relation with the magnetic field along the *x*-axis. The ME coupling constants are obtained by evaluating the slope of these plots. Interestingly, we found a very large electronic ME coupling response in SIO–BTO, β^{e}_{zx} = −1.7 ps m^{-1}. This electronic ME response is five times larger than the theoretical values of many conventional ME materials, *e.g.* Cr_2O_3 (0.35 ps m^{-1} calculated using the same approach, which agrees well with the data in ref. 16). We believe that this large ME coupling is related to the strong SOC in iridate-based superlattices. The ionic ME coupling constant β^{i}_{zx} is found to be −1.9 ps m^{-1}, which is larger than that of Cr_2O_3. In fact, to the best of our knowledge, this ionic or lattice ME constant is the largest ME coupling constant ever reported. Incorporating the electronic contribution, the total ME coupling in SIO–BTO significantly increases to −3.6 ps m^{-1}. According to the ME coupling tensor of SIO–BTO shown earlier, the other non-zero component (β^{i}_{xz}) is also calculated. The ionic polarization of SIO–BTO as a function of *z*-axis magnetic field is plotted in Fig. 3(b), where a moderate ME coupling constant of 0.44 ps m^{-1} is obtained. For the latter case, we found no response on the electronic polarization; hence, the electronic ME coupling constant (β^{e}_{xz}) is zero.

In our study, we used the magnetic field as a stimulus because it modifies the magnetic moments *via* Zeeman energy, which subsequently changes the charge distribution as well as the electronic wave functions. This alters the polarization *via* spin–orbit coupling and the large ME coupling in SIO–BTO is related to the strong SOC in iridates. Indeed, the presence of ionic polarizations in these oxide superlattices is vital to acquire a direct ME coupling. To confirm the critical role of polarizations, similar ME coupling calculations are performed for SIO–STO superlattice, which does not possess a polarization. All electronic and ionic components of the ME coupling do not show any significant response, revealing the importance of ionic polarizations for ME coupling in the systems.

The effects of epitaxial strains on the ME coupling constants of the SIO–BTO superlattice are also determined. Different in-plane lattice parameters are used to mimic the effects of epitaxial strains. Specifically, the crystal structures of strained SIO–BTO are first optimized, then the ME coupling constants are calculated. We investigated in-plane tensile and compressive strains of 0.25% and −0.25%, respectively. We found that the magnitude of the electronic ME coupling of SIO–BTO under compression is 1.78 ps m^{-1} (Table 2). This value is higher than the corresponding electronic ME coupling of equilibrium SIO–BTO, implying that compressive strain increases the magnitude of β^{e}_{zx}. On the contrary, when the

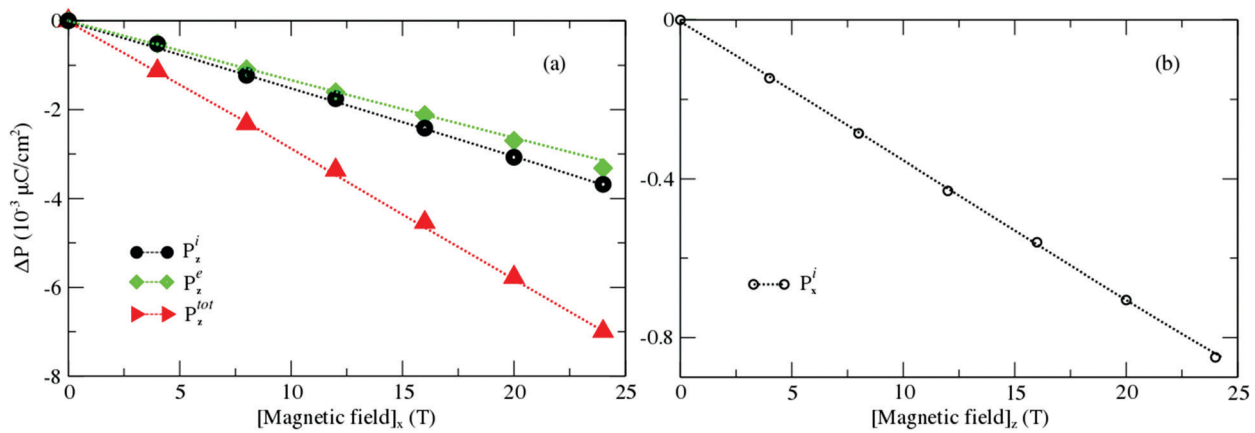

Fig. 3 (a) The changes in the polarization of the SIO–BTO in response to a magnetic field directed along the *x*-axis. The diamond and circle symbols represent the variations in the electronic and ionic polarization, respectively, and triangles represent changes in the total polarization. The rest of the ME coupling constants in the matrix are found to be essentially zero, which agrees with the analysis based on the magnetic symmetry group. (b) The variations of ionic polarizations along the *x*-axis as a function of the magnetic fields applied along the *z*-axis. The magnetic fields along the *z*-axis could not alter the electronic polarizations for this case.

Table 2 The electronic and ionic magnetoelectric coupling constants of SIO–BTO under epitaxial strains

	Electronic ME coupling constants	Ionic ME coupling constants	
Strain (%)	β^{e}_{zx} (ps m^{-1})	β^{i}_{zx} (ps m^{-1})	β^{i}_{xz} (ps m^{-1})
−0.25	−1.78	−1.91	−0.61
0.00	−1.71	−1.96	−0.44
0.25	−1.63	−2.32	−0.79

structure of SIO–BTO is exposed to the tensile strain, the absolute value of electronic ME coupling (β^{e}_{zx}) is reduced to 1.63 ps m^{-1}.

Interestingly, the ionic ME coupling β^{i}_{zx} shows the opposite dependence on the epitaxial strains, compared with the electronic ME component β^{e}_{zx}. As listed in Table 2, the magnitude of the ionic ME coupling constant (β^{i}_{zx}) of SIO–BTO superlattice increases with tensile strain. The ionic ME coupling constant can be as large as 2.32 ps m^{-1} per unit cell with a 0.25% tensile strain, an increase of 0.26 ps m^{-1}. In comparison, under the same tensile strain, the electronic ME coupling constant is decreased by 0.12 ps m^{-1}. Therefore, we conclude that the epitaxial strain has a larger impact on the ionic component of the ME coupling constants (β^{i}_{zx}) than the corresponding electronic component. We have also investigated the effect of strain on the other non-zero component of the ME coupling tensor for SIO–BTO superlattice, β^{i}_{xz}, and we found that both compressive and tensile strains increase the ME coupling constants. In fact, tensile strain increases β^{i}_{xz} by almost two times, which is the largest relative increase we observed in our study.

In a comparative study, the ME coupling of SIO–CTO is also computed. The magnetic point group of SIO–CTO is m' and it has five non-zero ME coupling constants in the ME coupling tensor, as shown below:

$$\beta = \begin{pmatrix} \beta_{xx} & 0 & \beta_{zx} \\ 0 & \beta_{yy} & 0 \\ \beta_{xz} & 0 & \beta_{zz} \end{pmatrix}$$

Therefore, the non-zero components are β_{xx}, β_{yy}, β_{zz}, β_{zx} and β_{xz}. In Fig. 4(a), we have plotted the change in the polarization of SIO–CTO *versus* magnetic fields. The ionic ME coupling constants are found to be β^{i}_{zx} = 0.86 ps m^{-1} and β^{i}_{xx} = −0.47 ps m^{-1}. In addition, the electronic ME coupling constant is β^{e}_{zx} = 0.2 ps m^{-1}. The ME coupling constant β^{e}_{xx} is zero. We have also evaluated the ME coupling when the SIO–CTO is exposed to a magnetic field along the *z*-axis (Fig. 4(b)) and found the same order of ME coupling constants. The ME coupling constant is β^{i}_{xz} = 0.8 ps m^{-1}. These values of the ME coupling constant are relatively smaller than those of SIO–BTO. Further investigation is needed to fully understand the differences in ME coupling exhibited by these systems.

IV. Summary

In summary, we determined ME coupling tensors in iridate-based oxide superlattices and found a surprisingly large ME coupling in SIO–BTO superlattice. Unlike other conventional materials, the electronic and ionic contributions to ME coupling are both significant in SIO–BTO. Comparatively, the ME coupling in SIO–CTO is moderate. By examining the electronic and ionic contributions as well as analyzing the structural distortion modes in superlattices, we believe that the large ME response in SIO–BTO is associated with a relatively high polarization of SIO–BTO and a strong SOC, which mediates the coupling between ionic displacements with the AFM spin configuration that senses external magnetic field through a spin-canting-induced net moment. In addition, we found that epitaxial strain can be used as an effective means to further tune the ME coupling. These results demonstrate the impact of SOC, structural distortions, and epitaxial strains on the ME coupling and provide insights to search for other materials with desired ME coupling properties or to enhance ME coupling effects in existing materials for practical applications.

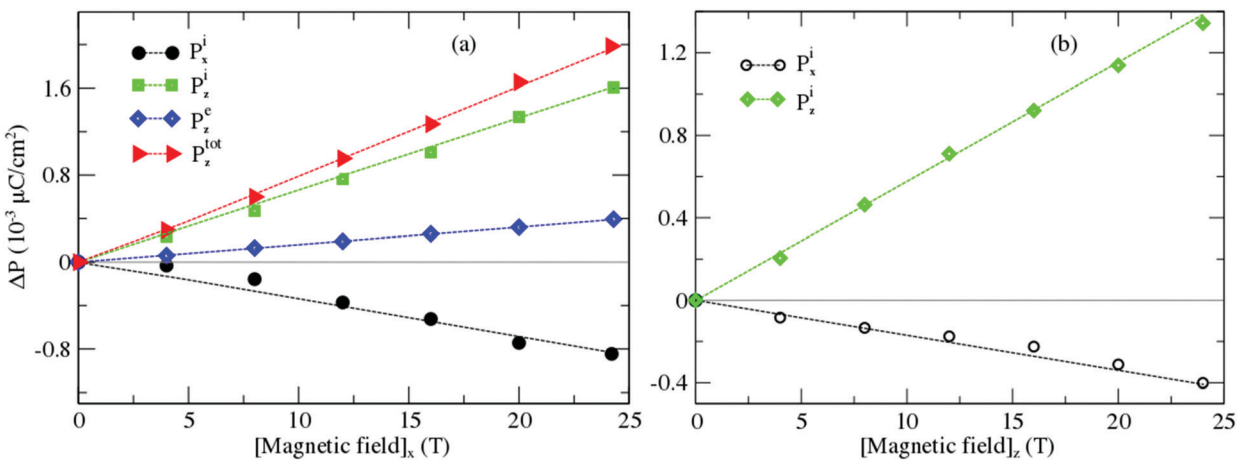

Fig. 4 The change in the polarization of the SIO–CTO as a function of the magnetic field. (a) The variations of the electronic and ionic polarizations while the magnetic field is directed along the *x*-axis. (b) The magnetic-field-induced polarizations in SIO–CTO when the magnetic field is parallel to the *z*-axis. The electronic ME coupling constants not presented in this figure have zero values.

Conflicts of interest

There are no conflicts to declare.

Acknowledgements

H. X. and J. L. acknowledge the support by the DoD-DARPA under Grant No. HR0011-16-1-0005 and the support by the Organized Research Unit Program (ORU-IMHM-18) at the University of Tennessee. J. L. acknowledges support by the National Science Foundation under Grant No. DMR-1848269. This research used the resources of the UT Advanced Computing Facility.

References

1 O. O. Brovko, P. Ruiz-Díaz, T. R. Dasa and V. S. Stepanyuk, Controlling magnetism on metal surfaces with non-magnetic means: electric fields and surface charging, *J. Phys.: Condens. Matter*, 2014, **26**, 093001.
2 M. F. Nicola and A. Spaldin, The Renaissance of Magnetoelectric Multiferroics, *Science*, 2005, **309**, 391.
3 T. R. Dasa and V. S. Stepanyuk, Direct surface charging and alkali metal doping for tuning interlayer magnetic order in planar nanostructures, *Phys. Rev. B: Condens. Matter Mater. Phys.*, 2015, **92**, 075412.
4 H. W. Jang, S. H. Baek, D. Ortiz, C. M. Folkman, R. R. Das, Y. H. Chu, P. Shafer, J. X. Zhang, S. Choudhury, V. Vaithyanathan, Y. B. Chen, D. A. Felker, M. D. Biegalski, M. S. Rzchowski, X. Q. Pan, D. G. Schlom, L. Q. Chen, R. Ramesh and C. B. Eom, Strain induced polarization rotation in epitaxial $BiFeO_3$ thin films, *Phys. Rev. Lett.*, 2008, **101**, 107602.
5 A. C. Garcia-Castro, A. H. Romero and E. Bousquet, Strain engineered multiferroicity in Pnma $NaMnF_3$ Flouproviskite, *Phys. Rev. Lett.*, 2016, **116**, 117202.
6 C. J. Fennie, Ferroelectrically Induced Weak Ferromagnetism by Design, *Phys. Rev. Lett.*, 2008, **100**, 167203.
7 T. Birol, N. A. Benedek, H. Das, A. L. Wysocki, A. T. Mulder, B. M. Abbett, E. H. Smith, S. Ghosh and C. J. Fennie, The Magnetoelectric effect in transition metal oxide: Insight and the rational design of new materials from first principles, *Solid State Mater. Sci.*, 2012, **16**, 227.
8 S. Picozzi, K. Yamauchi, B. Sanyal, I. A. Sergienko and E. Dagotto, Dual nature of improper ferroelectricity in magnetoelectric multiferroic, *Phys. Rev. Lett.*, 2007, **99**, 227201.
9 E. Bousquet and N. Spaldin, Induced Magnetoelectric response in Pnma perovskite, *Phys. Rev. Lett.*, 2011, **107**, 197603.
10 T. Varga, A. Kumar, E. Vlahos, S. Denev, M. Park, S. Hong, T. Sanehira, Y. Wang, C. J. Fennie, S. K. Streiffer, X. Ke, P. Schiffer, V. Gopalan and J. F. Mitchell, Coexistence of weak ferromagnetism and ferroelectricity in the high pressure $LiNbO_3$-type phase of $FeTiO_3$, *Phys. Rev. Lett.*, 2009, **103**, 047601.
11 N. A. Benedek and C. J. Fennie, Hybrid improper ferroelectricity: A mechanism for controllable polarization and magnetization, *Phys. Rev. Lett.*, 2011, **106**, 107204.
12 S. Ghosh, H. Das and C. J. Fennie, Linear magnetoelectricity at room temperature in perovskite superlattice by design, *Phys. Rev. B: Condens. Matter Mater. Phys.*, 2015, **92**, 184112.
13 J. M. Rondinelli and C. J. Fennie, Octahedral rotation-induced ferroelectricity in cation ordered perovskites, *Adv. Mater.*, 2012, **24**, 1961.
14 E. Bousquet, M. Dawber, N. Stucki, C. Lichtensteiger, P. Hermet, S. Gariglio, J. M. Triscone and P. Ghosez, Improper ferroelectricity in perovskite oxide artificial superlattice, *Nature*, 2008, **452**, 732.
15 J. Iniguez, First principle approach to lattice mediated magnetoelectric effects, *Phys. Rev. Lett.*, 2008, **101**, 117201.
16 E. Bousquet, N. A. Spaldin and K. T. Delaney, Unexpectedly large electronic contribution to linear magnetoelectricity, *Phys. Rev. Lett.*, 2011, **106**, 107202.
17 F. Ricci and E. Bousquet, Unveiling room temperature magnetoelectricity of Troilite FeS, *Phys. Rev. Lett.*, 2016, **116**, 227601.
18 A. Scaramucci, E. Bousquet, M. Fechner, M. Mostovoy and N. A. Spaldin, Linear magnetoelectric coupling by orbital magnetism, *Phys. Rev. Lett.*, 2012, **109**, 197203.
19 L. Y. Wei, C. Lian and S. Meng, Prediction of two-dimensional electron gas mediated magnetoelectric coupling at ferroelectric $PbTiO_3/SrTiO_3$ interface, *Phys. Rev. B: Condens. Matter Mater. Phys.*, 2017, **95**, 184102.
20 J. M. Rondinelli, M. Stengel and N. A. Spaldin, Carrier mediated magnetoelectricity in complex oxide heterostructures, *Nat. Nanotechnol.*, 2008, **3**, 46.
21 L. Hao, D. Meyers, H. Suwa, J. Yang, C. Frederick, T. R. Dasa, G. Fabbris, L. Horak, D. Kriegner, Y. Choi, J.-W. Kim, D. Haskel, P. Ryan, H. Xu, C. Batista, M. Dean and J. Liu, Giant magnetic response of a two dimensional antiferromagnet, *Nat. Phys.*, 2018, **14**, 806.
22 G. Jackeli and G. Khaliullin, Mott insulators in the strong spin-orbit coupling limit: From Heisenberg to a quantum compass and Kitaev models, *Phys. Rev. Lett.*, 2009, **102**, 017205.
23 W. Witczak-Krempa, G. Chen, Y. B. Kim and L. Balents, Correlated quantum phenomena in the strong spin-orbit regime, *Annu. Rev. Condens. Matter Phys.*, 2014, **5**, 57–82.
24 J. G. Rau, E. K.-H. Lee and H.-Y. Kee, Spin-Orbit Physics Giving Rise to Novel Phases in Correlated Systems: Iridates and Related Materials, *Annu. Rev. Condens. Matter Phys.*, 2016, **7**, 195–221.
25 G. Kresse and J. Furthmueller, Efficient iterative scheme for ab-initio total energy calculations using a plane wave basis set, *Phys. Rev. B: Condens. Matter Mater. Phys.*, 1996, **56**, 11169.
26 P. E. Blöchl, Projector augmented wave method, *Phys. Rev. B: Condens. Matter Mater. Phys.*, 1994, **50**, 17953.
27 J. P. Perdew, A. Ruzsinszky, G. I. Csonka, O. A. Vydrov, G. E. Scuseria, L. A. Constantin, X. Zhou and K. Burke, Restoring the density gradient expansion for exchange in solids and surfaces, *Phys. Rev. Lett.*, 2008, **100**, 136406.
28 J. Bertinshaw, Y. K. Kim, G. Khaliullin and B. J. Kim, Square Lattice Iridates, *Annu. Rev. Condens. Matter Phys.*, 2019, **10**, 315–336.
29 P. Guss, M. E. Foster, B. M. Wong, F. P. Doty, K. Shah, M. R. Squillante, U. Shirwadkar, R. Hawrami, J. Tower and

D. Yuan, Results for aliovalent doping of $CeBr_3$ with Ca^{2+}, *J. Appl. Phys.*, 2014, **115**, 034908.

30 M. Cococcioni and S. de Gironcoli, Linear response approach to the calculation of the effective interaction parameters in the LDA+*U* method, *Phys. Rev. B: Condens. Matter Mater. Phys.*, 2005, **71**, 035105.

31 B. Kim, P. Liu and C. Franchini, Dimensionality strain phase diagram of strontium iridates, *Phys. Rev. B: Condens. Matter Mater. Phys.*, 2017, **95**, 115111.

32 L. Zhang, B. Liu, H. Zhuang, P. R. C. Kent, V. R. Cooper, P. Ganesh and H. Xu, Oxygen vacancy diffusion in bulk $SrTiO_3$ from density functional theory, *Comput. Mater. Sci.*, 2016, **118**, 309.

33 T. R. Dasa, L. Hao, J. Yang, J. Liu and H. Xu, Strain effects on structural and magnetic properties of $SrIrO_3/SrTiO_3$ superlattice, *Mater. Today Phys.*, 2018, **4**, 43.

34 R. D. King-Smith and D. Vanderbilt, Theory of polarization crystalline solids, *Phys. Rev. B: Condens. Matter Mater. Phys.*, 1993, **47**, 1651.

35 C. Capillas, E. Kroumova, M. I. Aroyo, J. M. Perez-Mato, H. T. Stokes and D. M. Hatch, SYMMODES: a software package for group theory analysis structural phase transition, *J. Appl. Crystallogr.*, 2003, **36**, 953.

36 I. Dzyaloshinsky, A thermodynamic theory of ''weak'' ferromagnetism of antiferromagnets, *J. Phys. Chem. Solids*, 1958, **4**, 241.

37 T. Moriya, Anisotropic superexchange interaction and weak ferromagnetism, *Phys. Rev.*, 1960, **120**, 91–98.

38 G. Cao, J. Bolivar, S. McCall, J. E. Crow and R. P. Guertin, Weak ferromagnetism, metal-to-nonmetal transition, and negative differential resistivity in single-crystal Sr_2IrO_4, *Phys. Rev. B: Condens. Matter Mater. Phys.*, 1998, **57**, R11039–R11042.

39 B. J. Kim, H. Ohsumi, T. Komesu, S. Sakai, T. Morita, H. Takagi and T. Arima, Phase-Sensitive Observation of a Spin-Orbital Mott State in Sr_2IrO_4, *Science*, 2009, **323**, 1329–1332.

40 J. Matsuno, K. Ihara, S. Yamamura, H. Wadati, K. Ishii, V. V. Shankar, H. Y. Kee and H. Takagi, Engineering a Spin-Orbital Magnetic Insulator by Tailoring Superlattices, *Phys. Rev. Lett.*, 2015, **114**, 247209.

41 L. Hao, D. Meyers, C. Frederick, G. Fabbris, J. Yang, N. Traynor, L. Horak, D. Kriegner, Y. Choi, J.-W. Kim, D. Haskel, P. J. Ryan, M. P. M. Dean and J. Liu, Two-Dimensional J_{eff} = 1/2 Antiferromagnetic Insulator Unraveled from Interlayer Exchange Coupling in Artificial Perovskite Iridate Superlattices, *Phys. Rev. Lett.*, 2017, **119**, 027204.

42 G. Cao, Y. Xin, C. S. Alexander, J. E. Crow, P. Schlottmann, M. K. Crawford, R. L. Harlow and W. Marshall, Anomalous magnetic and transport behavior in the magnetic insulator $Sr_3Ir_2O_7$, *Phys. Rev. B: Condens. Matter Mater. Phys.*, 2002, **66**, 214412.

43 J. W. Kim, Y. Choi, J. Kim, J. F. Mitchell, G. Jackeli, M. Daghofer, J. van den Brink, G. Khaliullin and B. J. Kim, Dimensionality Driven Spin-Flop Transition in Layered Iridates, *Phys. Rev. Lett.*, 2012, **109**, 037204.

